Generation of High-Precision DEMs of the Wadden Sea with Airborne Interferometric SAR[*]

Christian Wimmer, Robert Siegmund, Marcus Schwäbisch, João Moreira

Aero-Sensing Radarsysteme GmbH
c/o DLR, D-82234 Oberpfaffenhofen, Germany
Phone: +49-8153-281611
Fax: +49-8153-281543
Email: Christian.Wimmer@dlr.de

March 27, 2000

Abstract

This paper describes how high-precision DEMs are obtained over the Wadden Sea using the AeS-1 airborne interferometric radar. The Wadden Sea is an intertidal zone along the coast which has height variations less than 5 m over 30 km and is free of vegetation. The resulting DEM has a grid spacing of 2.5 m and an absolute height accuracy of 5 cm rms, as verified by theodolite measurements. The paper describes the radar system, the processing techniques, the test area, the results, and the verification procedure.

1 Introduction

Interferometric synthetic aperture radar systems (InSAR) have become an important tool for generating digital elevation models (DEM) and orthorectified SAR images. The application field not only covers the tropical areas with absence of topographic maps but also areas in industrial countries. They need high resolution digital elevation models, city models, and the update of the existing cartographic information. High resolution DEMs are mainly obtained from photogrammetric and laser scanner systems that have a height accuracy as good as 15 cm [1].

The airborne InSAR systems CCRS C/X SAR [2], TOPSAR [3], DO-SAR [4], IFSARE [5], E-SAR [6], and EMISAR [7] have demonstrated the capability to generate digital elevation models with a height accuracy in an order of magnitude of meters. This paper presents the experience gained with the AeS-1 system for generation of DEMs of flat terrain with an absolute height error of 5 cm (1σ).

The SAR data used in this study were acquired over the German Bight near the city of Bremerhaven. This area is a part of the German "Wadden Sea", which is an intertidal zone along the coast. This zone is temporarily flooded and is separated into tidal flats that fall dry, and tidal channels that remain filled with water during a tidal cycle. The topography over this area is usually flat over tens of kilometers. Height variations depend on the distribution of the tidal inlets and the distribution of the typical sediments like mud and sand. Basically, this distribution is effected by tidal currents and wave action.

Due to these currents and wave action the topography of these areas is highly dynamic. Consequently the changes in morphology have to be observed accurately, e.g. to maintain the waterways that connect the harbours at the coast to the North Sea. For those observations hydrodynamic models are maintained, which need the surface topography as one boundary condition. Surveying the topography in that areas is a difficult task. Because the terrain is temporarily flooded, shallow, and very wide spread, it is difficult to conduct a survey neither from the ship nor by terrestrial methods. For this purpose airborne radar interferometry provides the derivation of high precision terrain height over wide areas in a convenient time period.

This paper is organized as follows: the AeS-1 system is presented in the next section, the precision processing is described in section 3 followed by a detailed evaluation of the height accuracy in section 4. Finally, the results and conclusions are presented.

2 The AeS-1 System

2.1 System Overview

In the beginning of 1996, Aero-Sensing Radarsysteme GmbH started to design and construct a high-resolution X-Band interferometric SAR called AeS-1 [8]. After first test flights in August 1996, the system became operational in October of the same year. Since then, the AeS-1 system has been used for various mapping campaigns all over the world. In the following, an outline of the system design and its actual performance is given.

The AeS-1 system basically consists of a ground and a flight segment. The block diagram in Fig. 1 shows their components and interconnections. The ground segment includes a GPS ground station for differential GPS measurements, a mobile computer for flight planning, and the transcription, archiving and SAR processing subsystems.

The core module of the flight segment is the radar itself (Fig. 2). It operates at a center frequency of 9.55 GHz with a maximum bandwidth of 400 MHz, thus enabling the acquisition of SAR images with a best-case ground resolution of 0.5 m. The transmitter/receiver unit uses a high precision local oscillator, a digital chirp generator and a TWT based output amplifier. High speed circulators allow a fully interferometric operation up to a pulse repetition frequency of 16 kHz. Raw data are stored on-board on hard disk arrays with a capacity of 432 GByte. With a maximum recording data rate of 32 MByte/s a total acquisition time of nearly 4 hours can be realized.

Three antennas are mounted on the aircraft, forming interferometric baselines of 0.6 and 2.4 m (Fig. 3). Currently, only two of them can be operated simultaneously, but in the near future a third channel will be implemented for further flexibility regarding to the operating modes as well as system calibration. The radar is automatically controlled by a flight control system which delivers the aircraft position in real-time with an absolute accuracy of 1 m so that the pilot can keep the position error between real and nominal track below 10 m during the entire flight.

Typically, AeS-1 is flown on a Rockwell Aero Commander 690 at flight heights of 3000 ... 8000 m. Operating costs can be kept low by the use of such a small aircraft, which can be flown by one pilot only. Nevertheless, high flexibility in selecting the flight height for specific purposes (e.g. lower altitudes for high resolution, high altitudes for wide swaths and less air turbulence) is guaranteed.

Tab. 1 summarizes the main parameters of the AeS-1 system.

2.2 Radar Accuracy

For obtaining high precision digital elevation models one has to fulfill three main criteria:

- *low radar phase noise:* The phase noise is mainly caused by the internal phase jitter of the radar and by the thermal noise. The phase jitter of the AeS-1 has a standard deviation of $0.5°$ and was measured by analysing the raw data of the backscattered signal of a corner reflector by a stationary measurement. The phase noise caused by the thermal noise depends on the signal-to-noise ratio (SNR). We have designed the system for having a nominal SNR over the Wadden Sea of 30 dB. A value of 30 dB causes an interferometric phase noise with a standard deviation of $5.5°$ (Fig. 4, [9]).

- *accurate and large baseline:* The three antennas for forming the small and large baselines are mounted in a rigid steel structure. On this structure the inertial navigation system (INS) is also mounted. The phase center of the antennas was measured in a near field antenna laboratory with an accuracy of 0.1 mm. The determination of the position and axis orientation of the measurement center of the INS was carried out using a precision table and the theodolite technique to achieve an accuracy of $0.01°$ in the axis orientation and 0.1 mm in the position. The baseline between the antennas and the INS was measured using the theodolite technique that also has an accuracy of 0.1 mm. The in-flight baseline changes due to the temperature variations are calculated by measuring the temperature in different parts of the structure. The large baseline, which was used for this experiment, has a length of 2.4 m and was the largest one that could be built for this aircraft. For low resolution applications the small baseline of around 0.6 m is used.

- *accurate motion data:* Both position and rotation of the antenna structure have to be measured so that the position and the Doppler centroid of the antennas can be determined accurately. We use the INS and the global positioning system (GPS) techniques as a combined solution. Using two GPS ground stations and carrying out differential and coherent GPS processing (D-GPS) one gets after post-processing an absolute position accuracy of around 3 cm (1σ) for a range between aircraft and GPS groundstation lower than 50 km and a good satellite constellation. The bandwidth of the GPS data is around 0.5 Hz and it is quite low for the SAR requirements [10]. The INS, which is based on accelerometers and dry tuned gyroscopes, is the source of accurate information of the rotation and the relative position, as it has a high bandwidth, for example 20 Hz in our case. A processing algorithm

then merges the data of both systems and the final absolute position and rotation data are related to a certain point fixed somewhere on the structure. The absolute accuracy of the final position data is the same as that of the D-GPS. The absolute accuracy of the rotation data is $0.003°$ and the relative one is $0.0003°$ (both values supplied by the manufacturer). This relative accuracy is valid over a time period of 10 minutes. By analysing the height information obtained by several corner reflectors placed over the range swath we can compensate the rotation offset and achieve an absolute accuracy of the rotation data of $0.0003°$. This procedure is presented in section 3.4.

3 Precision Processing

The block diagram of the processor is shown in Fig. 5. The following subsections explain the individual steps, which are: SAR processing, interferometric processing, phase filtering, absolute phase estimation, geocoding, and mosaicking.

3.1 SAR Processing

The SAR processor has the following steps:

1. *Demultiplexing the raw data:* The raw data are first demultiplexed in order to separate the raw data of each antenna. Both antenna signals are first processed separately to be combined later on at the interferometric step.

2. *Antenna position and Doppler centroid calculation:* The position and rotation data of the navigation system are used to calculate the position of the phase center of both antennas by using the respective lever arms. The Doppler centroid is range dependent and calculated separately for both antennas.

3. *Range Compression:* It is carried out in the frequency domain and uses the chirp replica as a reference function.

4. *Primary motion compensation:* It is called primary due to the fact that the terrain model is not known and the topography used is given by the earth ellipsoid including the local mean terrain height. This approximation is corrected later after obtaining the first order DEM by applying a secondary motion compensation. The correction method of the primary motion compensation is given in [11].

5. *Azimuth Compression:* A hybrid correlation algorithm is used for the azimuth compression. This algorithm uses a frequency domain fast correlation in the azimuth direction, with a time domain convolution operation in the range dimension, in order to handle the finite amount of dispersion of the azimuth reference function due to the range migration. It works in the squinted geometry, which is defined by the range dependent Doppler centroid calculated before. The output of the azimuth compression is a single look complex (SLC) image.

3.2   Interferometric Processing

After SAR focusing, two SLC datasets enter the interferometric processor. Its task is to extract each target's phase signature from both channels and combine them coherently to form an unwrapped phase difference image (interferogram) with the best possible SNR. The basic processing steps are image co-registration, interferogram formation, and phase unwrapping, which are implemented using standard algorithms. Note, that unlike the typical satellite case no spectral shift filtering [12] is necessary since the interferometric baseline is only 3% of its critical value ($\simeq 80$ m for 3 km flight height and $30°$ incidence angle (near range)). Furthermore, spectral filtering in azimuth is not needed since both antennas have the same pointing with respect to the flight direction.

However, in order to achieve the required high phase accuracy, the conventional co-registration step had to be modified. As will be discussed later (4.1.1) a geometric misregistration can introduce a significant phase bias (and hence height error) in the case of a squinted observation geometry. Therefore, a very accurate estimation of the slave image shift had to be achieved. In order to reduce errors in the measurement of the image shift the following strategy was applied:

1. In a first step the registration parameters are estimated for each part of each track ($\simeq 2$ km$\times 2$ km) separately. Here a conventional correlation technique in the time domain is applied, yet with the restriction that the shift parameters are constant over azimuth. This assumption holds as long as both antenna tracks are parallel to each other and have a constant height over ground. Both requirements are fulfilled for the Wadden Sea data: in the motion compensation the ideal tracks are defined to be parallel to each other, they are defined to have a constant height over the reference ellipsoid, and the terrain showed extremely low height variations (less than 5 m over the entire area) so that it can be considered as flat.

2. Again exploiting the fact that the imaging geometry is constant along the azimuth direction, the individual shift parameters are then averaged in order to reduce statistical measurement errors.

3.3   Phase Filtering

The raw interferometric phase, which is represented in slant range geometry, contains artifacts and noisy areas that are inconvenient for the end user. The aim of this filter is to prepare the raw interferometric phase in such a form that the resulting DEM is as close as possible to the real topography.

For that purpose we developed a filter that is optimized for filtering the interferometric phase obtained from the flat area of the Wadden Sea. Other terrain types will certainly require another filter configuration.

The Wadden Sea area itself is flat having a height variation of less than 5 m over 30 km. Phase unwrapping errors are not present, which is a reliable assumption. However, the following interferometric phase features do not correspond to the real topography:

1. *Phase spikes:* The Wadden Sea area has innumerous tidal inlets, whose structure is formed like that of small "canyons". If their orientation is parallel to the flight direction the radar signal suffers from multiple reflections. The corresponding interferometric phase looses the relationship to the real topography. This phenomenon comes out in the form of phase spikes, which have several radians of amplitude.

2. *Phase with high thermal noise:* Due to the periodic flooding, the slicky areas remain wet forming a kind of dense suspension. This leads to a very smooth surface for most wind conditions. In an extreme situation one can find nearly a specular reflection in that area. As a consequence, the backscattered signal has a low amplitude and the thermal noise influence becomes remarkable and the standard deviation of the phase error increases.

For the above mentioned phase features we have implemented the corresponding filters:

1. *Spike filter:* This filter consists of a sigma filter, a coherence threshold operator, and an interpolator. The sigma filter detects the phase spikes and masks the corresponding pixels. The coherence threshold operator masks all pixels which are lower than a certain coherence threshold and are in the neighbourhood of the pixels masked by the sigma filter in order to eliminate phase errors in these

surroundings. For this threshold we chose a value of 0.85 which guarantees that all unreliable phase information is discarded. Thereafter a triangulation algorithm interpolates the masked areas.

The phase spikes themselves are small spots (typically of 10 m diameter) and their number is small as well so that the percentage of the area masked is less than 1%. Note, that the accuracy of the DEM is not decreased due to this filtering since the spatial bandwidth of the topography is at least twenty times lower than the DEM sampling of 2.5 m.

2. *Thermal noise filter:* It is implemented after the phase is spike-filtered. The thermal noise filter is a low pass filter whose cutoff frequency depends on the standard deviation of the thermal noise. By adjusting the cutoff frequency according to the standard deviation of the thermal noise, one can obtain an interferometric phase whose error has a constant standard deviation.

   If the area has a high backscatter coefficient, the cutoff frequency is set to infinity, i.e. the low pass filter is turned off. In this case the output phase remains unfiltered and presents a phase error with a nominal standard deviation. The nominal standard deviation is derived in 4.1.3. The complex interferogram is low pass filtered with a cutoff spatial frequency of $1/5 \text{ m}^{-1}$ obtaining 100 looks from the original interferogram with 0.5 m geometric resolution. Finally, we obtain a standard deviation which is equal to $0.56°$ (see section 4.1.3).

   If the area has a low backscatter coefficient, the cutoff frequency is set to such a value, that the standard deviation of the phase noise remains constant to $0.56°$ degrees. This compensation degrades the geometric resolution. By defining a lower limit of geometric resolution we determine the lowest coherence where the filter is effective. The lowest acceptable geometric resolution was set to 60 m $\times$ 60 m, i.e. to a number of looks of 14,400. Now, the operating range of the filter can be derived. With 14,400 looks one is able to reduce a maximum phase standard deviation of $66°$ to $0.56°$. According to [9] we get this phase noise for a SNR of 3.15 dB, see Fig. 4. For this SNR level we get a correlation coefficient of 0.33. That means, that the cutoff spatial frequency varies in a range of $1/5 \text{ m}^{-1}$ to $1/60$ m^{-1} for a coherence range of 0.99 to 0.33.

3.4 Absolute Phase Estimation

The phase offset for estimating the absolute phase is an essential parameter in interferometry and has to be determined very accurately. Starting point is a precisely known trigonometric point close to the region of interest. This point is used for determining the position of the corner reflectors which are placed along the range direction of one of the flight tracks. The measurement of the corner positions is done using the static D-GPS technique, where a long measuring time guarantees a high accuracy down to 1 cm. In this way we obtain precise reference points which are used for the phase offset calculation of the so-called "corner track" by forward or backward geocoding (Eqs. 1...5 in section 3.5).

In the absence of corner reflectors the phase offset is determined using the elevation information of an overlapping geocoded track that serves as a reference DEM. A final adjustment of the phase offset is done by an iterative procedure until the slope of the difference between geocoded and reference DEM is less than 5 cm in 2 km. This criterion can only be reached if the roll angle does not have an offset higher than $0.0003°$, which is necessary for achieving the 5 cm DEM accuracy (see section 4.2). The roll angle offset which is given by the absolute angle accuracy, i.e. it can be within $\pm 0.003°$, is in turn determined by the residual slope according to Eq. 9. Thereafter, a final adjustment of the phase offset eventually needs to be carried out.

Following these calibration steps, a secondary motion compensation has to be done since the primary motion compensation (3.1) was carried out without considering the topography. For this secondary motion compensation three steps have to be performed:

1. conversion of the interferometric phase into height

2. compensation of the remaining height errors:

   - The interferometric phase errors caused by the primary motion compensation are calculated by comparing the slant range height with the mean terrain height

   - The interferometric phase errors are converted into height and used to correct the slant range height

3. conversion of the improved slant range height image into a cartographic reference system

9

3.5 Height Derivation and Geocoding

The derivation of geocoded height information is carried out by solving the standard range/Doppler equations and the ellipsoid equation [13]:

$$2 \left(\vec{P} - \vec{S}_1 \right) \left(\dot{\vec{P}} - \dot{\vec{S}}_1 \right) = \lambda \, r_1 \, f_{DC_1} \tag{1}$$

$$\left| \vec{P} - \vec{S}_1 \right| = r_1 \tag{2}$$

$$2 \left(\vec{P} - \vec{S}_2 \right) \left(\dot{\vec{P}} - \dot{\vec{S}}_2 \right) = \lambda \, r_2 \, f_{DC_2} \tag{3}$$

$$\left| \vec{P} - \vec{S}_2 \right| = r_1 + \frac{\lambda}{4\pi} \Phi \tag{4}$$

$$\frac{P_x^2 + P_y^2}{a^2} + \frac{P_z^2}{b^2} = 1 \tag{5}$$

where
λ = radar wavelength

$f_{DC_{1,2}}$ = Doppler centroid frequencies

r_1 = range distance of master image pixel

$\vec{P}$ = requested pixel's location

$\vec{S}_{1,2}$ = antenna positions

$\dot{\vec{P}}, \dot{\vec{S}}_{1,2}$ = derivatives with respect to time

Φ = pixel's interferometric phase

a, b = semi-major and semi-minor ellipsoid axis

Simultaneous solution of Eqs. 1...4 for each image pixel directly leads to its location in the preselected geodetic reference frame. Alternatively, a two-step procedure consisting of phase-to-height conversion (Eqs. 1, 2, and 5) and subsequent backward geocoding (Eq. 3) can be applied if the slant range height is required.

3.6 Mosaicking

The investigated area was imaged with two orthogonal crossing tracks, each of them flown three times (for results see section 5). Accordingly, each region was mapped three times at least and six times at best.

The final elevation model is composed by mosaicking and averaging the stack of these individual elevation layers, using weights in order to further improve the height accuracy. In addition to the final DEM, a height accuracy map and a reliability map is generated.

3.6.1 Mosaicked DEM

For each final image pixel the ultimate height value is calculated from all available input values using the following two-step procedure:

1. first the values are arranged according to their magnitude, then all values with deviations from the centre value (median) larger than a certain threshold are discarded from the stack. In that way possible outliers are rejected from the averaging process.

2. the remaining values are weighted according to their accuracy, and the final result is calculated as the weighted average of the input values. The input accuracy is taken from the local coherence of the interferogram, which is a measure for the statistical rms height accuracy of the data. Values with systematic errors, which still may be present in the single height layers, are expected to be discarded by the previous median operation.

The mosaicked elevation map then is finally corrected by subtracting the geoid undulations which specify the height difference between the geoidal and ellipsoidal heights. Although only in the cm-range, the geoid undulations have to be removed to allow a comparison to theodolite measurements (section 5).

3.6.2 Height accuracy map

The height accuracy of the mosaicked and averaged DEM is calculated as a weighted mean of the individual improvements $v_i = \bar{x} - x_i$:

$$\sigma = \sqrt{\frac{\sum_{i=1}^{n} p_i \, v_i \, v_i}{(n-1) \sum_{i=1}^{n} p_i}} \tag{6}$$

where
n = number of observations
x_i = single height value
$\bar{x}$ = mean height value
p_i = weight

11

3.6.3 Reliability map

The so-called *reliability* has been introduced as a further quality criterion which, besides the weighting of the individual measurements, additionally incorporates the number of observations. A low reliability indicates a high probability for one (or more) of the observations to be outliers. Reliability estimation is based on χ^2 statistics and is reported in detail in [14].

4   Evaluation of the Height Accuracy

We distinguish between errors coming from the radar itself and errors that are induced by the navigation system.

4.1   Radar-induced Phase Errors

Radar phase errors and their impact on the accuracy of the interferometric height can be divided into two classes:

- systematic phase errors, causing a phase bias

- statistical phase errors, which reduce the phase SNR and can be decreased by adequate low-pass filtering

4.1.1   Systematic phase errors

The geometric misregistration of the SLCs can be identified as the main systematic error for AeS-1 data. In the typical airborne case of a squinted imaging geometry and squint processing, the system's impulse response function is characterized by a linear phase ramp which causes an interferometric phase bias $\delta\Phi$ if both channels are not perfectly registered [15]:

$$\delta\Phi = \frac{4\pi}{\lambda}\delta x \ (1 - cos\beta) \tag{7}$$

where δx = misregistration

      β = squint angle

Subsequently, a misregistration of only 1/10 of the resolution cell of AeS-1 (0.5 m) already results in a phase bias of 18° at a squint value of 10°. Accordingly, accurate co-registration is an absolute requirement for precise elevation derivation. Using the improved registration algorithm (section 3.2), a registration accuracy better than 0.01 resolution cells (i.e., 5 mm) has been realized. With the actually flown squint angles of 2.5°, a phase error of 0.45° rms was obtained. Note, that co-registration for terrain types with significant slopes may require modified algorithms in order to achieve the 0.01 accuracy value (e.g. co-registration using a first-order interferometric DEM).

4.1.2 Statistical phase errors

Statistical errors in AeS-1 data mainly emerge from three sources:

- *Receiver phase noise:* has been proven to be less than 0.5° (see section 2.2).

- *Defocusing of SLCs:* phase noise introduced through imperfect processing of the raw data [9] has been measured to be less than 0.5°.

- *Decorrelation of echoes from both antennas:* due to the single-pass characteristic of AeS-1, no temporal decorrelation is present. However, signal decorrelation may occur for the following reasons:

    - thermal noise: over the Wadden Sea area a signal-to-noise ratio of 30 dB is obtained. Following the investigations of [9] a phase standard deviation of 5.5° results (Fig. 4).

    - layover/shadowing effects: areas affected by these events are identified during image processing, and dummy values are assigned to them in the single elevation layers. In the final mosaicking step (see section 3.6) gaps are filled with data from opposite look directions.

    - volume decorrelation: is only of minor importance for the small X-Band wavelength. Generally, coherence is lowered slightly in forested areas, however those are not present in the investigated area.

4.1.3 Phase error budget

Combining all radar-induced phase errors, we obtain a total rms value of 5.56°, which is only slightly higher than its main contribution (5.5° coming from the signal-to-noise ratio). This value reduces to 0.56° due to the fact that the image resolution is decreased to 5 m × 5 m by interferogram multilooking.

The impact of interferometric phase errors on the height accuracy is described by the following relation between phase noise $\delta\Phi$ and resulting height error δh [16]:

$$\delta h = \frac{\lambda\, r\, (\sin\theta + \cos\theta\ \tan\tau_y)}{4\pi\, B_\perp}\, \delta\Phi \tag{8}$$

where r = slant range between sensor and target ($\simeq 4.2$ km)

            θ = look angle of observation ($\simeq 45°$)

            τ_y = terrain slope in range direction ($\simeq 0°$)

            λ = radar wavelength (3.1 cm)

            $B_\perp$ = baseline orthogonal to look direction (1.9 m)

            (the values indicated in parenthesis are representative for AeS-1, mid range, Wadden Sea data)

Accordingly, a rms height error of 3.7 cm is caused by radar-induced phase errors.

4.2 Navigation System-induced Phase Errors

The main error sources of the navigation system that cause a height degradation in the final terrain model are the absolute height and the absolute roll angle errors [17]:

- *Aircraft absolute height:* it has a direct influence on the height of the final terrain model. The navigation system based on D-GPS/INS data can deliver the absolute height with an error less than 3 cm ($1\,\sigma$), which is mainly defined by the D-GPS height error, if it operates under optimum conditions.

- *Aircraft roll angle:* the roll angle error strongly influences the height accuracy due to the long lever arm between the radar and the ground. A roll angle error $\delta\gamma$ causes a rotation of the entire DEM with lever arm r about the roll axis. Accordingly, the height error δh results as the projection of this displacement onto the vertical:

$$\delta h = \sin\theta_i\, r\, \delta\gamma \tag{9}$$

where θ_i indicates the incidence angle. $\delta\gamma$ has a standard deviation of $0.0003°$ for the case that we determine the roll angle offset through several corner reflectors or through a precise terrain model. If there is no calibration of the roll offset angle, the standard deviation of $\delta\gamma$ is $0.003°$. Considering the

system as calibrated and the mid range case, i.e. a range of 4200 m and an incidence angle of 45°, the standard deviation of the height error δh due to roll angle errors is 1.6 cm.

4.3   Total Height Error Budget

Combining all error sources discussed in the previous sections, which we summarize as

- radar-induced noise $\Rightarrow$ 3.7 cm
- GPS error $\Rightarrow$ 3 cm
- roll angle error $\Rightarrow$ 1.6 cm

a total height error of 5.02 cm results.

5   Results

The data presented in this paper were acquired on a flight in September 22, 1998 over the Wadden Sea near to the city of Bremerhaven in northern Germany. Two different tracks crossing each other were recorded. Each track was flown three times at different flight altitudes (1500 m, 2200 m, and 3000 m) to ensure data redundancy, which is used for quality improvement. Fig. 6 shows the ortho-rectified SAR amplitude of one of the tracks, extending over 2 km × 6 km and indicating the typical characteristics of the area with its numerous tidal channels. In Fig. 7 the interferometric phase of a 2 km × 2 km part of the area is displayed, Fig. 8 shows the corresponding coherence. Note that particularly the inundated parts are characterized by low coherence, whereas most of the dry areas show coherence values close to 1.

The tracks were geocoded and finally mosaicked to obtain a DEM whose outer dimensions extend over a 5 km × 5 km area. The DEM's grid size was set to 2.5 m according to the customer's requirements. In Fig. 9 the mosaicked elevation map consisting of the two crossing tracks is shown. The terrain height over the entire area varies between -3 m and +2 m. Fig. 10 displays height contour lines that have been automatically derived from the DEM. Their contour interval is 20 cm.

Four profiles taken from the AeS-1 DEM are indicated in Figs. 9 and 10. They are plotted in Fig. 11

along with reference profiles obtained by theodolite measurements. These reference measurements were carried out by the Federal Waterway Engineering and Research Institute (BAW) two weeks before the radar acquisition, a time period which is sufficiently short in order to guarantee comparable measurements. The black line in Fig. 11 represents the reference profile obtained with the theodolite, the upper and lower blue lines denote a respective ±10 cm offset. It can be seen that the AeS-1 DEM measurements, shown in red, are within the ±10 cm limits over almost the entire range, and they never exceed a 20 cm deviation. The standard deviations of the difference between the AeS-1 profiles and the theodolite measurements are reported in Tab. 2. A mean standard deviation of 5.9 cm is obtained by combining all difference measurements.

6 Experience with other Terrain Types

Although the paper is focused on the DEM generation of flat and vegetation-free intertidal zones like the Wadden Sea, which is a rather ideal testsite for interferometric DEM generation, we want to give a brief overview over the obtainable accuracy over other terrain types.

Tab. 3 reports the height accuracies that have been obtained with AeS-1 data over terrain with different kinds of vegetation coverage and topographic characteristics. During flight campaigns in Switzerland, Brazil, and The Netherlands, vegetated areas with flat as well as hilly topography have been imaged. A vertical accuracy between 17 cm and 25 cm has been obtained. The DEMs have been validated against different kinds of reference information, namely D-GPS measurements, trigonometric points, and laser scanning measurements.

7 Conclusions

The airborne interferometric SAR technique, in this paper represented by the AeS-1 system, shows an unique capability for obtaining exceptionally high precision DEMs of relatively flat and vegetation-free terrain like the Wadden Sea area. No other remote sensing sensors like the photogrammetric and laser scanner systems are capable of getting such a height accuracy and geometric resolution in this type of terrain [18][19]. Also the all-weather capability and automated procedure for processing and geocoding the radar raw data lead to low costs for the production of such high accurate DEMs.

For obtaining such a height accuracy the following conditions have to be fulfilled:

- accurate position and angle data from the navigation system

- radar with low phase noise and with well-known antenna baselines

- motion compensation procedure has to consider the effects of the topography

- flat terrain with only sparse vegetation coverage (e.g. intertidal areas, grassland)

The height accuracy over land is typically degraded by the presence of vegetation and topography. Despite the advantage of significantly higher reflection over vegetated areas, topography variations prevent the usage of strong interferometric filters, e.g. 5 m × 5 m as used for the Wadden Sea case, leading to height accuracies in the order of 20 cm.

8   Acknowledgements

References

[1] U. Lohr, "Digital elevation models by laser scanning," *Photogrammetric Record*, vol. 16(91), pp. 105–109, Apr. 1998.

[2] A. L. Gray and P. J. Farris-Manning, "Repeat-pass interferometry with airborne synthetic aperture radar," *IEEE Trans. on Geoscience and Remote Sensing*, vol. 31, pp. 180–191, Jan. 1993.

[3] H. A. Zebker, S. N. Madsen, J. Martin, K. B. Wheeler, T. Miller, Y. Lou, G. Alberti, S. Vetrella, and A. Cucci, "The TOPSAR interferometric radar topographic mapping instrument," *IEEE Trans. on Geoscience and Remote Sensing*, vol. 30, pp. 933–940, Sept. 1992.

[4] N. P. Faller and E. H. Meier, "First results with the airborne single-pass DO-SAR interferometer," *IEEE Trans. on Geoscience and Remote Sensing*, vol. 33, pp. 1230–1237, Sept. 1995.

[5] J. B. Mercer and A. Kahil, "RADARSAT and IFSARE - complementary SAR sources for DEMs," in *Proceedings of the First Latino-American Seminar on Radar Remote Sensing - Image Processing Techniques*, (Buenos Aires), pp. 47–52, 1997. (ESA SP-407).

[6] R. Scheiber, A. Reigber, K. P. Papathanassiou, R. Horn, S. Buckreuß, and A. Moreira, "Overview of interferometric data acquisition and processing modes of the experimental airborne SAR system of DLR," in *Proceedings of IGARSS'99*, (Hamburg), pp. 35–37, 1999.

[7] S. N. Madsen, N. Skou, K. Woelders, and J. Granholm, "EMISAR sinlge pass topographic SAR interferometer modes," in *Proceedings of IGARSS'96*, (Lincoln), pp. 674–676, 1996.

[8] M. Schwäbisch and J. Moreira, "The high resolution airborne interferometric SAR AeS-1," in *Proceedings of the Fourth International Airborne Remote Sensing Conference*, (Ottawa), pp. I–540 – I–547, 1999.

[9] D. Just and R. Bamler, "Phase statistics of interferograms with applications to synthetic aperture radar," *Applied Optics*, vol. 33, no. 20, pp. 4361–4368, 1994.

[10] J. Hepburn, B. Reid, W. Widnall, D. Liang, and G. Haslam, "Motion compensation for high resolution spotlight SAR," in *Proceedings of IEEE Position, Location, and Navigation Symposium (PLANS'84)*, (San Diego), pp. 59–65, 1984.

[11] J. Kirk, "Motion compensation for synthetic aperture radar," *IEEE Trans. on Aerospace and Electronic Systems*, vol. 11, no. 3, pp. 338–348, 1975.

[12] F. Gatelli, A. M. Guarnieri, F. Parizzi, P. Pasquali, C. Prati, and F. Rocca, "The wavenumber shift in SAR interferometry," *IEEE Trans. on Geoscience and Remote Sensing*, vol. 32, pp. 855–865, July 1994.

[13] F. Holecz, J. Moreira, P. Pasquali, S. Voigt, E. Meier, and D. Nüesch, "Height model generation, automatic geocoding and mosaicking using airborne AeS-1 InSAR data," in *Proceedings of IGARSS'97*, (Singapore), pp. 1929–1931, 1997.

[14] W. Baarda, "A testing procedure for use in geodetic networks," *Netherlands Geodetic Commission*, vol. 2, no. 5, 1968.

[15] M. Bara, R. Scheiber, and A. Broquetas, "Interferometric SAR signal analysis in the presence of squint," in *Proceedings of IGARSS'99*, (Hamburg), pp. 257–259, 1999.

[16] E. Rodriguez and J. M. Martin, "Theory and design of interferometric synthetic aperture radars," *IEE Proceedings-F*, vol. 139, pp. 147–159, Apr. 1992.

[17] S. N. Madsen, H. A. Zebker, and J. Martin, "Topographic mapping using radar interferometry: Processing techniques," *IEEE Trans. on Geoscience and Remote Sensing*, vol. 31, pp. 246–256, Jan. 1993.

[18] C. Wever, "Laserscannermessungen zur topographischen Geländeaufnahme." Oral presentation at *KÄFER - Küsten- und Ästuarfernerkundung*, workshop held in Hamburg, Germany, 27. April 1999.

[19] H. Heyer, "Aktuelle Fragen im Küstenwasserbau - Anforderungen an Qualität und Verfügbarkeit der Grundlagendaten." Oral presentation at *KÄFER - Küsten- und Ästuarfernerkundung*, workshop held in Hamburg, Germany, 27. April 1999.

[20] E. Meier, internal validation letter from RSL (Remote Sensing Laboratories), University of Zürich, Switzerland, Nov. 1999.

[21] V. Kirchhoff, internal validation letter from INPE (Instituto Nacional de Pesquisas Espaciais), S. José dos Campos, Brazil, May 1999.

[22] Grontmij Geogroep (Ed.), "Airborne InSAR demonstration for urban and rural applications", technical report of Grontmij Geogroep bv, The Netherlands, Dec. 1999.

Figure and Table Captions

Figure 1: Block diagram of AeS-1 ground and flight segments

Figure 2: AeS-1 flight segment

Figure 3: Aero Commander with 3 X-Band antennas

Figure 4: Interferometric phase standard deviation vs. signal-to-noise ratio

Figure 5: Block diagram of SAR and InSAR processor

Figure 6: SAR amplitude of a 2 km $\times$ 6 km strip of the Wadden Sea

Figure 7: Interferometric phase of a 2 km $\times$ 2 km part of the Wadden Sea area; scaling is from $-\pi$ to π

Figure 8: Coherence of same area as shown in Fig. 7; scaling is from 0 to 1

Figure 9: AeS-1 DEM

Figure 10: Height contour lines derived from the AeS-1 DEM with a contour interval of 20 cm

Figure 11: Height profiles taken from AeS-1 DEM (red) and from theodolite measurements (black)

Table 1: System parameters of AeS-1 X-Band system

Table 2: Standard deviation of height differences between AeS-1 DEM and theodolite profiles

Table 3: Height accuracy of AeS-1 DEMs obtained over different types of terrain
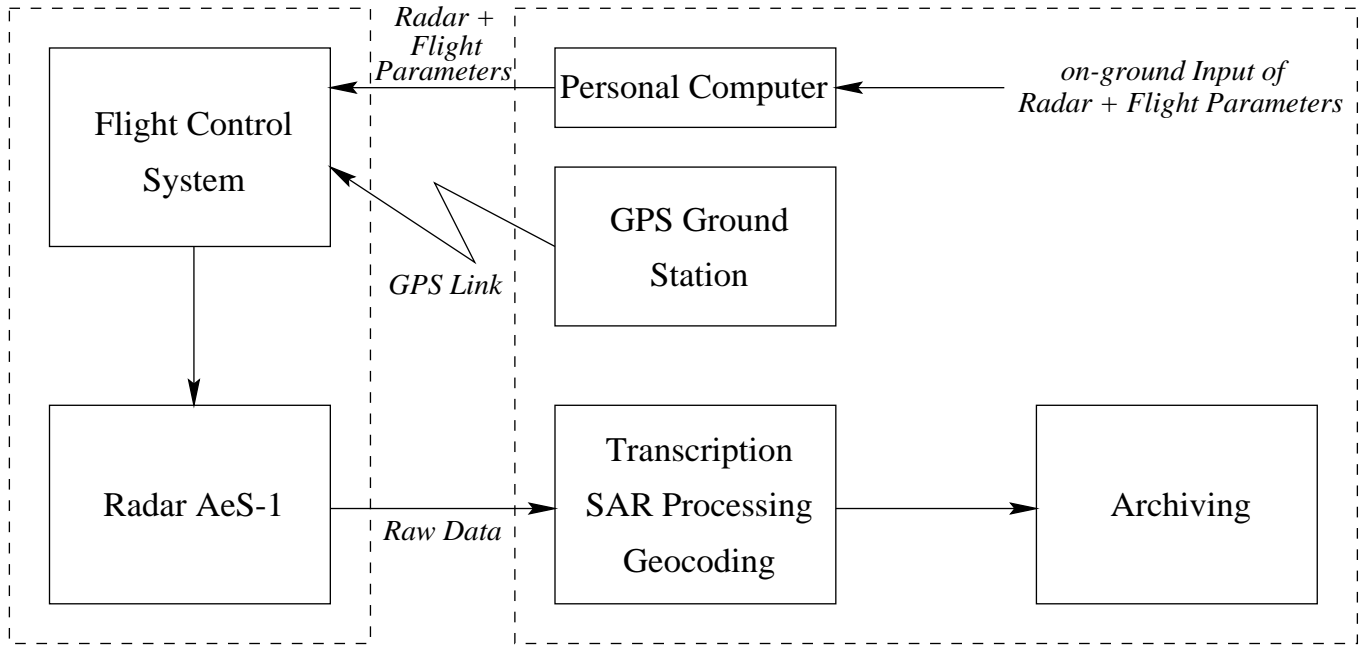
Flight Segment   **Ground Segment**
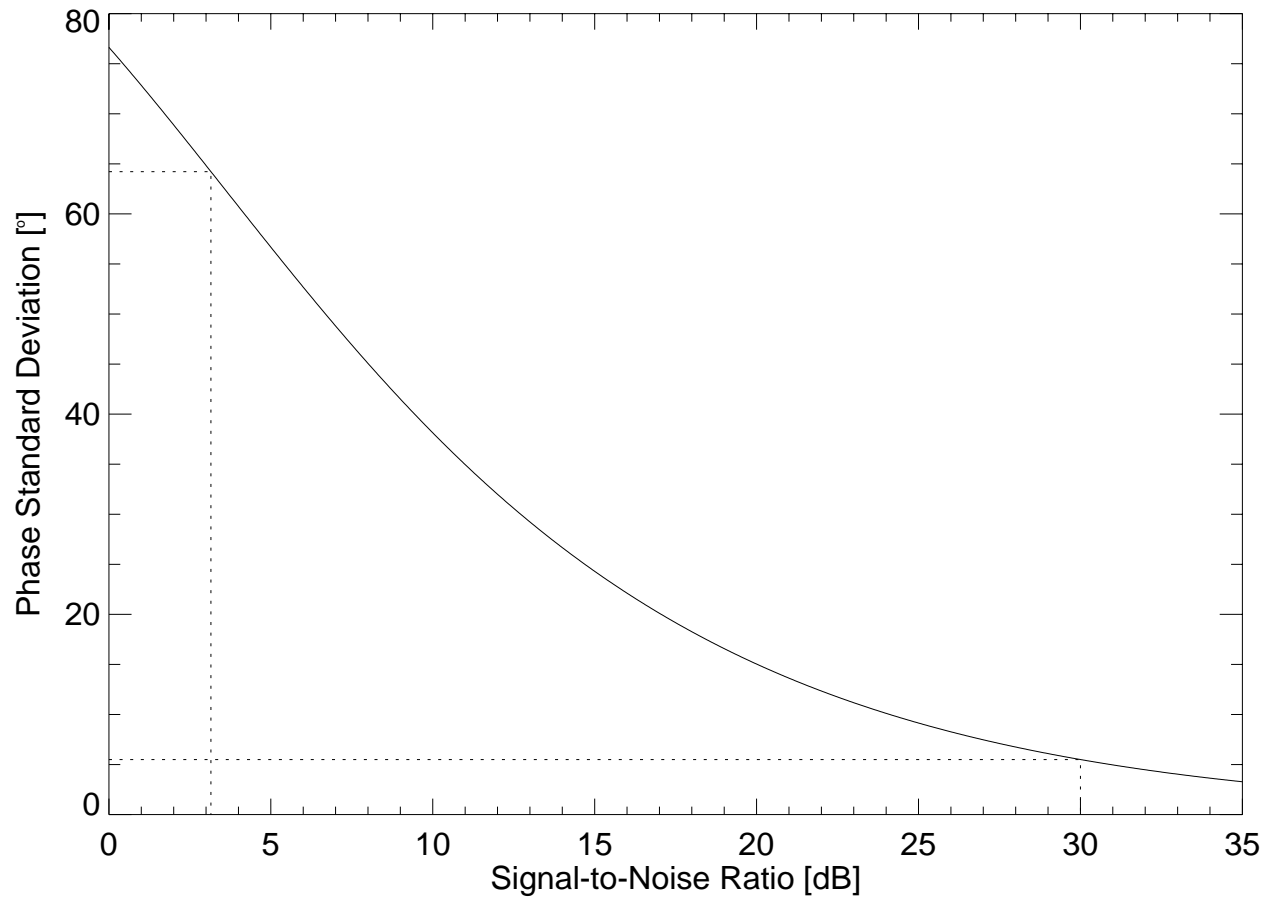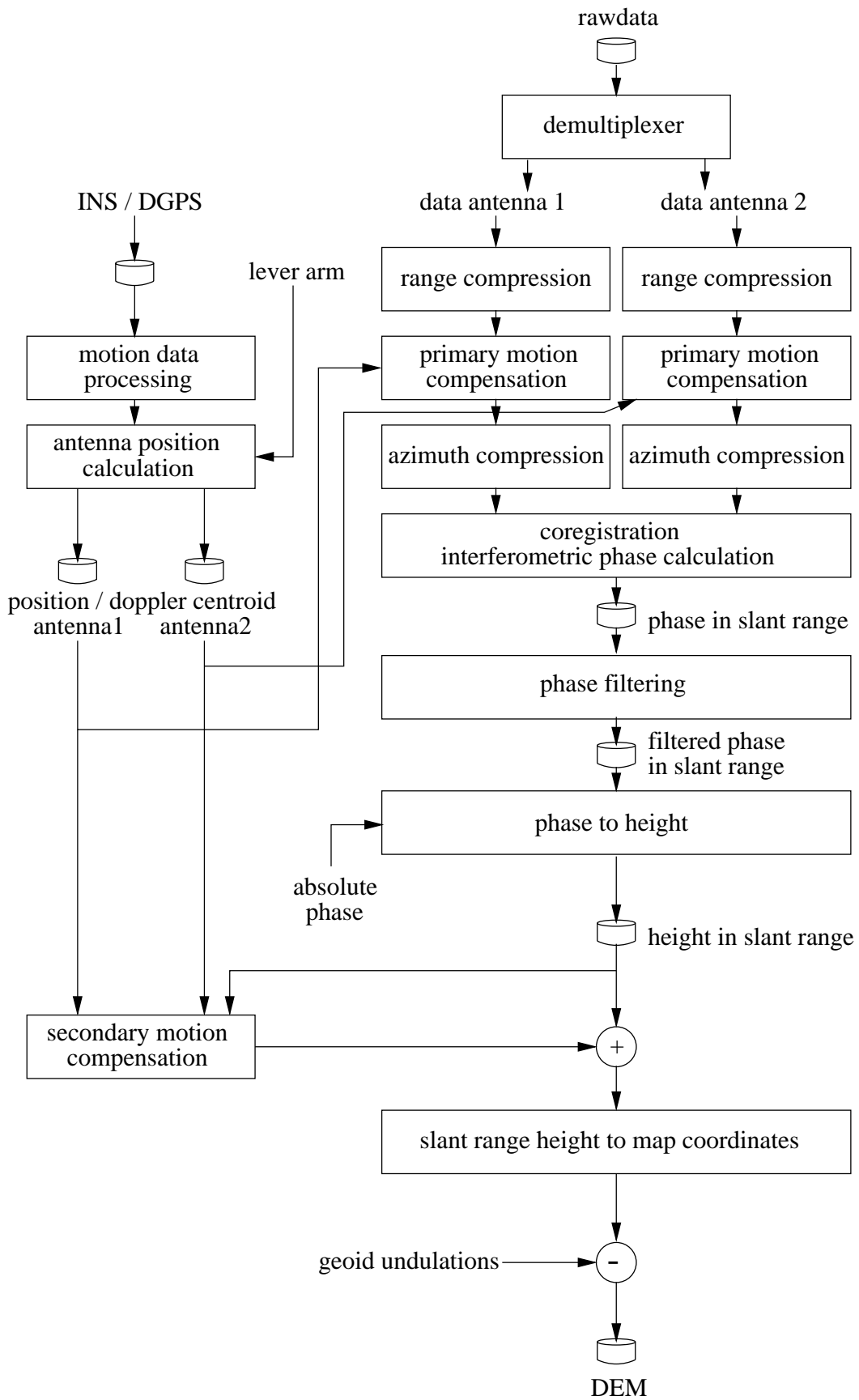

Fig. 1

Fig. 2

Fig. 3

Fig. 4

Fig. 5